RESEARCH PAPER

Influence of Sn and Al Doping on ZnO Thin Films: A Study of Structural, Optical, and Langmuir Adsorption Properties for Photocatalytic Applications

Aicha Kater[1], Saâd Rahmane[1], Fatima Djenidi[1], Hala Nezzal[2], Nourelhouda Mokrani[1], Elhachmi Guettaf Temam[1,*], Hadjer Barkat[1], Boutheina Saadi[1], Brahim Gasmi[1]

** elhachemi.guettaf@univ-biskra.dz*

[1] Physics Laboratory of Thin Films and Applications, Biskra University, BP 145 RP, 07000, Biskra, Algeria
[2] Physics Laboratory of Photonics and Multifunctional Nanomaterials, BP 145, RP, 07000, Biskra, Algeria

Received: June 2025 **Revised: August 2025** **Accepted: October 2025**
DOI: 10.22068/ijmse.4142

Abstract: *Zinc oxide (ZnO) thin films have garnered significant interest due to their applications in optoelectronics and environmental remediation, owing to their exceptional optical, electrical, and photocatalytic properties. However, the high resistivity and rapid charge recombination of pure ZnO necessitate doping to enhance its performance. In this study, ZnO thin films doped with tin (Sn) and aluminium (Al) were synthesised using a cost-effective pneumatic spray technique. The structural, optical, and morphological properties of the films were systematically characterized using X-ray diffraction (XRD), UV-Vis spectrophotometry, scanning electron microscopy (SEM), and energy-dispersive X-ray spectroscopy (EDX). The results indicate that Sn and Al doping significantly influence ZnO's crystallinity, bandgap energy, and surface morphology. The optimal crystallite size was obtained for 1 wt.% Sn (37.98 nm) and 5 wt.% Al (48.63 nm), while excessive doping (>3 wt.%) introduced microstrain (10.41×10^{-4} for Sn and 7.13×10^{-4} for Al), reducing crystallinity. The optical bandgap decreased from 3.254 eV (pure ZnO) to 3.142 eV (1 wt.% Sn) and 3.152 eV (5 wt.% Al), accompanied by increased Urbach energy (0.34 eV for 5 wt.% Al). The highest optical transmittance (86%) was observed for 3 wt.% Al-doped ZnO. Pure ZnO exhibited the highest photocatalytic efficiency, achieving 85% methylene blue degradation under solar irradiation. Langmuir adsorption modelling revealed that Sn-doped ZnO exhibited the highest adsorption capacity (1.422 mg/g), followed by Al-doped ZnO (0.617 mg/g) and pure ZnO (0.495 mg/g). These findings highlight the crucial role of doping concentration in optimising ZnO thin films for advanced photocatalytic and optoelectronic applications.*

Keywords: *ZnO thin films, Sn and Al doping, Pneumatic spray deposition, Structural characterization, Photocatalysis, Langmuir adsorption isotherm.*

1. INTRODUCTION

The development of semiconductor materials with enhanced properties is critical to addressing challenges in energy conversion, environmental remediation, and optoelectronics [1–3]. Zinc oxide (ZnO) has emerged as a highly versatile material due to its unique electrical, optical, and catalytic properties, making it widely applicable in fields such as transparent conductive oxides (TCOs), gas sensors, photovoltaics, and environmental remediation [4–6]. Its wide bandgap (3.1 eV) and high exciton binding energy contribute to its excellent optical transparency and stability, which are essential for optoelectronic applications [7–10]. However, pure ZnO suffers from inherent limitations, including relatively high resistivity and rapid charge recombination, which restrict its use in high-performance devices [11, 12].

To overcome these drawbacks, doping ZnO with metallic elements has been extensively explored [13–16]. Among these, aluminum (Al) and tin (Sn) are of particular interest due to their ability to modify ZnO's electrical, structural, and optical properties. Al-doped ZnO (AZO) is widely recognized as a low-cost and effective alternative to indium tin oxide (ITO) for transparent conductive films, owing to Al's ability to enhance carrier concentration while maintaining high transparency [17, 18]. Notably, AZO films deposited on grass-like alumina (GLA) showed a 228% increase in electrical conductivity, demonstrating the effectiveness of Al doping in improving ZnO's electrical properties [14]. On the other hand, Sn-doped ZnO (SZO) is known for its enhanced luminescence and field emission properties, attributed to the close ionic radii of Sn^{4+} (0.69 Å) and Zn^{2+} (0.74 Å), which allow for effective lattice substitution without severe structural distortion [18]. This structural compatibility ensures that Sn^{4+} incorporation into the ZnO lattice maintains its integrity while significantly improving luminescence", making SZO a promising material for optoelectronic applications [18, 19].

Various deposition techniques, including chemical vapor deposition (CVD), sol-gel spin coating, and

[DOI: 10.22068/ijmse.4142]

magnetron sputtering, have been employed to synthesize high-quality ZnO thin films.

However, these methods often require complex instrumentation, high-vacuum conditions, or costly precursors, which limits their large-scale applicability [20]. In contrast, the pneumatic spray technique presents a simple, cost-effective, and scalable alternative for depositing ZnO thin films with controlled thickness and uniformity [21]. This method enables the deposition of ZnO thin films over large areas, making it particularly advantageous for industrial applications, such as solar cells and optoelectronics [21]. Additionally, it provides precise control over film thickness and uniformity, ensuring desirable optical and electrical properties [21]. Despite its potential, limited research has systematically compared the effects of Sn and Al doping on ZnO thin films prepared using this method [22]. Doping ZnO with elements like Sn and Al can significantly alter its electrical and optical properties. However, the specific effects of these dopants when using the pneumatic spray technique are not well-documented, indicating a gap in current research [22]. Doping concentration also influences ZnO's structural integrity, potentially affecting its crystallinity and phase composition, which in turn impact its mechanical properties [22]. Moreover, optimizing doping levels is essential for maximizing the structural and functional properties of ZnO thin films, particularly for applications such as gas sensors and solar cells [21, 23, 24]. A comparative analysis of the pneumatic spray technique with other deposition methods in terms of efficiency, cost, and scalability is also needed, especially for doped ZnO thin films [20, 25]. Studies on ZnO doping often focus on single dopants or less scalable methods. Mo doping enhances photodetection by increasing the bandgap and carrier lifetime [26]. Al doping improves conductivity and transparency for solar cells [13]. Fe doping enhances photocurrent properties [27], while Sn doping increases carrier concentration and bandgap [28]. Scalable methods like spray pyrolysis [13], magnetron sputtering [28], and hybrid approaches ensure good conductivity and transparency [29], making ZnO films suitable for industrial applications.

This study systematically investigates the impact of Sn and Al doping on ZnO thin films synthesized via the pneumatic spray technique. By varying doping concentrations, we analyze how these dopants influence ZnO's structural, optical, morphological, and photocatalytic properties. Characterization techniques such as X-ray diffraction (XRD), UV-Vis spectroscopy, and scanning electron microscopy (SEM) provide detailed insights into changes in crystallinity, transparency, and surface morphology. Additionally, the Langmuir adsorption model was applied to evaluate the adsorption behavior of methylene blue (MB) on ZnO-based thin films, revealing that Sn-doped ZnO exhibited the highest adsorption capacity, followed by Al-doped and pure ZnO films. The results demonstrate that intrinsic ZnO exhibits the highest photocatalytic activity, while optimal doping levels enhance crystallization and optical transparency. Specifically, ZnO films doped with 1 wt.% Sn and 5 wt.% Al exhibits the best crystallization, whereas 3 wt.% Al-doped ZnO achieves the highest optical transmittance of 86%. These findings emphasize the crucial role of doping concentration in tailoring ZnO properties for various applications, offering a scalable and efficient route for fabricating high-performance ZnO-based thin films.

2. EXPERIMENTAL PROCEDURES

2.1. Materials

ZnO-based thin films were deposited on microscope glass slides (No. 7102, 25.4 × 76.2 × 1 mm). The slides were meticulously cleaned using a 10% acetic acid (CH_3COOH, A6283, ≥99%) solution in deionized water at 90°C to eliminate impurities and improve film adhesion. Deionized water was used for all experiments. Zinc chloride ($ZnCl_2$, 208086, reagent grade, ≥98%), Tin chloride dehydrates ($SnCl_2.2H_2O$, 243523, ACS reagent, 98%) and Aluminum chloride hexahydrate ($AlCl_3.6H_2O$, 237078, ReagentPlus, 99%) were used as the Zn, Sn and Al precursors, respectively. All chemicals were sourced from Sigma-Aldrich and were used without further purification to guarantee experimental reproducibility.

2.2. Synthesis of ZnO-Based Thin Films

Thin films of undoped ZnO, tin-doped ZnO (ZnO:Sn), and aluminium-doped ZnO (ZnO:Al) with different concentrations (1, 3 and 5 wt.%) were deposited using the pneumatic spray technique on glass substrates. Zinc chloride, $ZnCl_2$, was used as a source of zinc. 0.1 M of zinc chloride was dissolved in 50 ml of deionized

[DOI: 10.22068/ijmse.4142]

water. The specific amounts of tin and aluminium chloride were added to the previous solution. This solution was stirred for 30 min at room temperature to obtain a homogenous solution. The solution was then sprayed onto heated glass substrates (400°C), which were positioned 30 cm from the spray nozzle at atmospheric pressure (1 atm) for 3 min as the growth time (Fig. 1).

2.3. Film Characterization

The structural characterization of the films was performed using X-ray diffraction (XRD) with a Rigaku MiniFlex 600 system, utilizing CuKα radiation (λ= 1.541874 Å). Optical transmission spectra were obtained using a UV-Vis spectrophotometer (JASCO V-770). Microstructural analysis was conducted using scanning electron microscopy (SEM) coupled with energy-dispersive X-ray spectroscopy (EDX) for verification of chemical composition. The particle size distribution was calculated using ImageJ software based on 50 measurements. The thickness (d) of the thin film is measured by the gravimetry method using the relation [8]:

$$d = \frac{m}{\rho \times A} \quad (1)$$

where A, m and ρ, are the film material's surface area (cm^2), mass (g) and density (g/cm^3), respectively. The growth velocity (Gv) was determined using:

$$Gv = \frac{d}{t} \quad (2)$$

Where d represents the thickness (nm) and t is the deposition time (min). The average crystallite size (D) was estimated by the Scherrer's equation [30]:

$$D = \frac{0.9\lambda}{\beta\cos(\theta)} \quad (3)$$

where λ is the wavelength of the X-ray beam (nm), θ is the diffraction angle (°), and β is the Full Width at Half Maximum (FWHM) considered in radians. The micro-strain (ε) value was calculated using [16]:

$$\varepsilon = \frac{\beta \cos\theta}{4} \quad (4)$$

The optical band gap energy, E_g (eV), was estimated using Tauc's relation [15]:

$$(\alpha h\nu) = A\left(h\nu - E_g\right)^{\frac{1}{2}} \quad (5)$$

where A is a constant and hν is the photon energy (eV). Urbach energy, E_u (eV), was determined from:

$$\alpha = \alpha_0 \times \exp\left(\frac{h\nu}{E_U}\right) \quad (6)$$

Where α_0 is a constant, E_u characterizes the slope of the exponential edge. The value of E_u was obtained from the inverse of the slope of ln(α) versus (hν).

2.4. Photocatalytic Evaluation

The photocatalytic activity of the films was assessed by monitoring the degradation of methylene blue (MB) under solar irradiation. A stock solution of MB was prepared by dissolving 8 mg of the dye in 1 L of distilled water, followed by 10 minutes of stirring. Before exposure, the solution was left in the dark for 30 minutes to establish adsorption equilibrium. During photocatalysis, 2 mL samples were withdrawn at regular intervals (0, 1, and 2.5 hours).

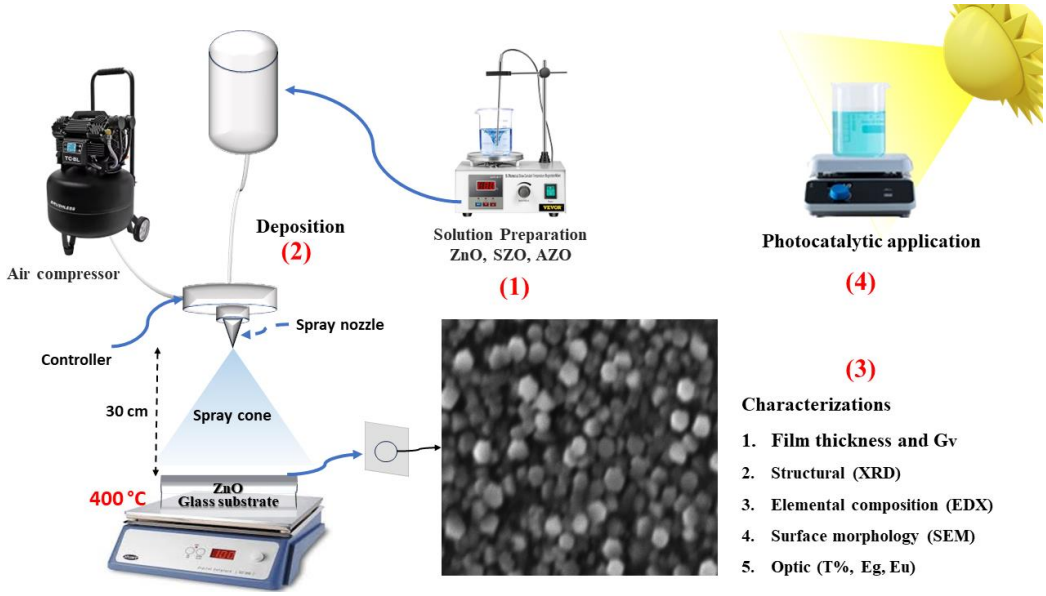

Fig. 1. Flowchart of the synthesizing and characterization process for ZnO-based thin films

[DOI: 10.22068/ijmse.4142]

The concentration changes were monitored via UV-Vis absorption spectroscopy. The degradation efficiency (η) was determined using:

$$\eta(\%) = \left(\frac{C_0 - C_t}{C_0}\right) \times 100 \quad (7)$$

where C_0 and C_t are the initial and time-dependent dye concentrations. The apparent rate constant (K_{app}) for the photodegradation reaction was calculated assuming first-order kinetics [31, 32]:

$$\ln\left(\frac{C_t}{C_0}\right) = -k_{app}.t \quad (8)$$

where t is the irradiation time (h). The slope of the linear fit of $\ln(C_t/C_0)$ versus t provides K_{app}. The determination coefficient (R^2) was used to evaluate the goodness of fit.

3. RESULTS AND DISCUSSION

Fig. 2(a) shows the effect of Sn doping on the thickness and growth velocity of ZnO thin films. Unlike Al-doped films, the thickness of Sn-doped ZnO films does not exhibit a continuous increase. Instead, it decreases significantly from 312.8 nm (undoped) to 133.1 nm at 1 wt.%, then increases to 229.8 nm at 3 wt.% before dropping again to 116.2 nm at 5 wt.%. This trend suggests that low and high Sn doping levels (1 wt.% and 5 wt.%) may introduce structural defects or disrupt the nucleation process, resulting in reduced film thickness, as observed in studies reporting increased resistivity and decreased crystallite size at higher doping concentrations [33, 34]. In contrast, intermediate concentrations (3 wt.%) may enhance grain growth and improve film density, as evidenced by Bi:SnO_2 films at 3 at% exhibiting the lowest sheet resistance and highest optical bandgap, indicating superior electrical and optical properties [33]. While intermediate doping levels yield optimal results, excessive doping can lead to undesirable effects such as increased resistivity and reduced optical clarity, which may limit the applicability of these materials in transparent conductive oxide applications [35]. Similarly, the growth velocity follows a comparable pattern, decreasing from 104.3 nm/min (undoped) to 44.4 nm/min at 1 wt.%, then recovering to 76.6 nm/min at 3 wt.%, before dropping again to 38.7 nm/min at 5 wt.%.

The variations observed can be rationalized by considering the effect of Sn concentration on the ZnO lattice. At low (1 wt.%) and high (5 wt.%) levels, the ionic radius mismatch between Sn and Zn induces local strain and defect states, which hinder uniform grain growth and reduce crystallinity. In contrast, at the intermediate concentration (3 wt.%), Sn incorporation is more homogeneous, minimizing lattice distortion and enabling improved grain alignment and crystallite growth. This interpretation is corroborated by the larger crystallite size (33.98 nm) and lower strain (10.21×10^{-4}) at 3 wt.% reported in Table 1, confirming that this doping level provides more favorable structural ordering [36,37].

Fig. 2(b) presents the thickness and growth velocity of ZnO thin films doped with Al at different concentrations. The thickness of the films initially decreases from 312.8 nm (undoped) to 235.6 nm at 1 wt.% Al doping but further decreases to 196.2 nm at 3 wt.%. However, at 5 wt.% doping, the thickness increases again to 256.8 nm. This increase at higher Al concentration suggests that Al^{3+} ions, due to their smaller radius compared to Zn^{2+}, generate compressive strain that modifies grain boundary mobility. This promotes secondary grain growth and induces a change in the preferential orientation of the crystallites. This behavior suggests that low Al concentrations can disrupt ZnO grain growth, leading to reduced film thickness, while higher doping levels (5 wt.%) may facilitate secondary grain growth or changes in crystal orientation [13,38].

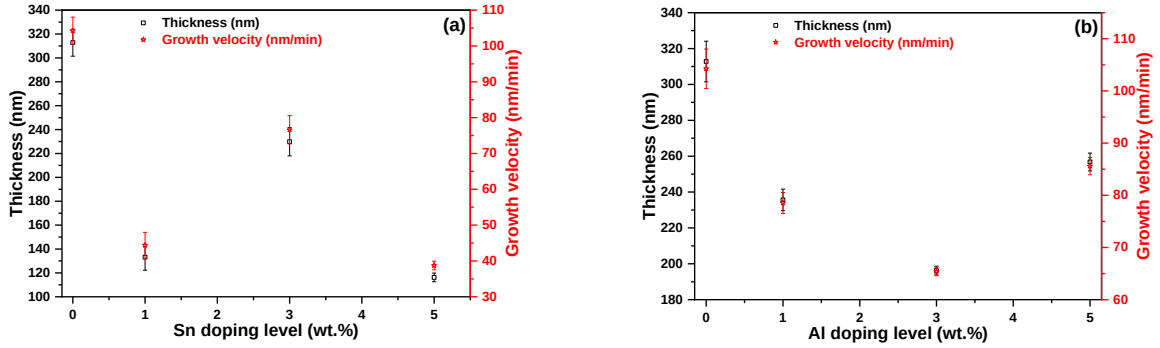

Fig. 2. Thickness and growth velocity of ZnO thin films doped with a) Sn and b) Al at different doping concentrations

[DOI: 10.22068/ijmse.4142]

Similarly, the growth velocity follows a comparable pattern, decreasing from 104.3 nm/min (undoped) to 78.5 nm/min at 1 wt.% and further to 65.4 nm/min at 3 wt.%, before rising again to 85.6 nm/min at 5 wt.%. The decrease at lower doping levels aligns with findings that Al incorporation initially inhibits grain boundary mobility, slowing deposition kinetics [38, 39]. The subsequent increase at 5 wt.% suggests that higher Al concentrations may alter surface energy and film stress, promoting enhanced growth [40]. These structural modifications highlight the importance of optimizing Al doping levels for achieving desirable ZnO thin-film properties [41].

Fig. 3(a) presents the X-ray diffraction (XRD) patterns of ZnO thin films doped with different concentrations of Sn. The pure ZnO film exhibits diffraction peaks corresponding to the hexagonal wurtzite structure, consistent with the JCPDS reference pattern (JCPDS No. 36-1451). The most intense peak is observed at $2\theta \approx 34.71°$, corresponding to the (002) plane, indicating a preferential c-axis orientation [42, 43]. Upon doping with 1 wt.% Sn, the intensity of the (002) peak decreases compared to pure ZnO, suggesting that the incorporation of Sn introduces additional lattice defects that disturb the long-range order. This behavior is due to the ionic radius mismatch between Sn^{4+} (0.69 Å) and Zn^{2+} (0.74 Å), which generates local strain and defects, hindering uniform lattice growth [44].

At 3 wt.% Sn, the (002) peak intensity increases again, indicating a partial recovery of crystallinity. This can be attributed to the more homogeneous incorporation of Sn into the ZnO lattice, where the ionic radius mismatch is minimised, thereby reducing strain and enabling improved structural alignment. As a result, the network distortion is less pronounced at 3 wt.% compared to the extremes of 1 wt.% and 5 wt.% doping. However, at 5 wt.% Sn, a further broadening and reduction of the (002) peak are observed. This indicates the onset of lattice distortion and the formation of microstrain and structural disorder due to the higher concentration of Sn. At this doping level, the ionic mismatch becomes more pronounced, introducing more defects and disturbing the crystallinity [45]. Additionally, the slight shift in the peak position at higher doping levels suggests minor modifications in lattice parameters due to the substitution of Zn^{2+} (ionic radius ~0.74 Å) by Sn^{4+} (~0.69 Å) or the possible formation of Sn-related defects within the ZnO matrix [46, 47]. The non-linear trend in the XRD data arises because, at lower doping concentrations (1 wt.%), the distortion is localized due to limited incorporation of Sn. At higher concentrations (5 wt.%), the lattice strain becomes more pronounced due to excessive dopant concentration. In contrast, at the intermediate 3 wt.% concentration, the doping is more homo-geneous, reducing distortion and enabling more ordered crystal growth, thus creating a recovery of crystallinity.

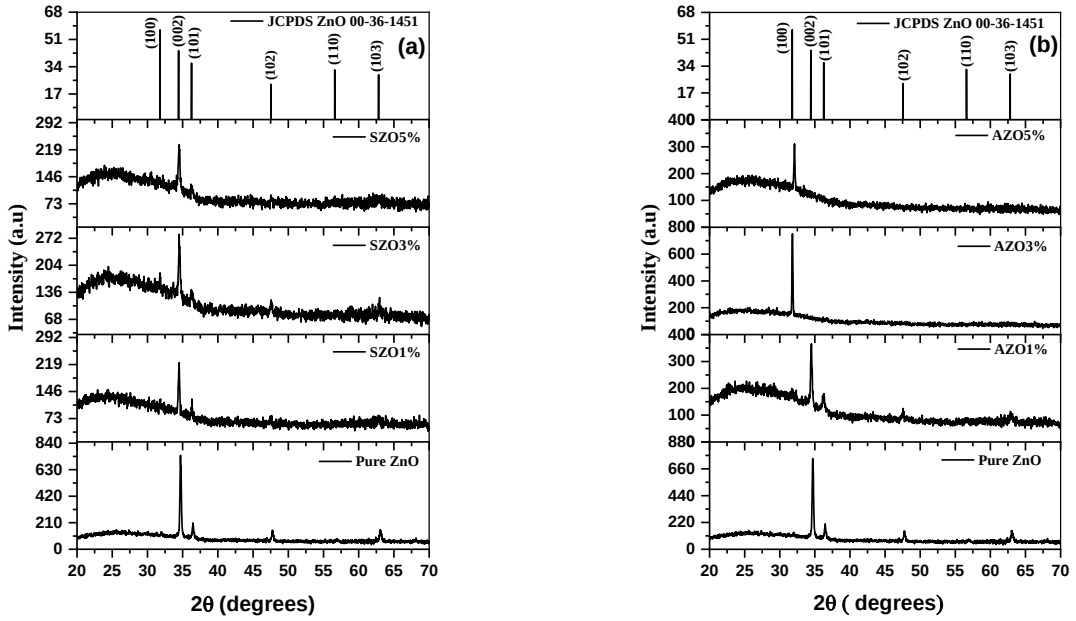

Fig. 3. X-ray diffraction (XRD) patterns of ZnO thin films doped with a) Sn and b) Al, showing characteristic diffraction peaks and changes in crystallinity

[DOI: 10.22068/ijmse.4142]

Fig. 3(b) shows the XRD patterns of ZnO films doped with Al, which match the hexagonal wurtzite structure (JCPDS No. 36-1451). The pure ZnO film exhibits a strong (002) peak at $2\theta \approx 34.71°$ (Table 1), confirming the preferential c-axis orientation [6, 46]. At 3 wt.% Al, the (002) peak weakens further, while the (100) peak at $2\theta \approx 31.77°$ becomes the most intense reflection, demonstrating a clear change in preferential orientation from (002) to (100) [48]. This orientation shift suggests that Al incorporation at intermediate concentrations significantly modifies growth dynamics, favouring the stabilization of the (100) plane. At 5 wt.% Al, the (002) peak remains weak and the (100) peak is still evident but with lower intensity compared to 3 wt.%, indicating that excessive Al incorporation introduces strain and structural disorder, which suppresses crystallinity [46, 48]. Peak broadening at these higher concentrations also reflects increased microstrain and defect density, further affecting film quality. These results show that moderate Al doping can drive a preferred orientation change, but higher concentrations disrupt the ZnO lattice and reduce overall crystallinity [46, 48].

Fig. 4(a) presents an enlarged view of the XRD patterns, focusing on the (002) diffraction peak of ZnO thin films doped with Sn. The pure ZnO film exhibits a sharp (002) peak at $2\theta \approx 34.71°$, which corresponds to the hexagonal wurtzite structure (JCPDS No. 36-1451). Babalola et al. [44] found that upon doping with 1 wt.% Sn, the (002) peak shifts slightly to a lower angle ($2\theta \approx 34.48°$), indicating an expansion of the c-axis lattice parameter. Sharma et al. [49] suggested that this shift confirms that Sn atoms are successfully incorporated into the ZnO lattice, slightly increasing the interplanar spacing due to local lattice distortions. However, at higher doping levels (3 wt.% and 5 wt.% Sn), the (002) peak shifts back toward higher angles ($2\theta \approx 34.53°$ and 34.50°, respectively), suggesting a partial relaxation of the lattice. Kumar et al. [45] and Boufelgha et al. [47] reported that this behavior can be attributed to a combination of factors, including the formation of Sn-related defects, lattice strain (Table 1), and possible Sn segregation at higher doping concentrations. Additionally, Boufelgha et al. [47] and Abdullah [46] confirmed that the broadening of the peak with increased Sn doping indicates a decrease in crystallite size, as shown in Fig. 5(a). Sharma et al. [49] and Boufelgha et al. [47] demonstrated that this reduction in crystallinity at higher Sn concentrations may negatively impact the film's electronic and photocatalytic properties by increasing defect density and charge recombination.

Fig. 4(b) provides an enlarged view of the (002) diffraction peak for Al-doped ZnO thin films. The pure ZnO sample exhibits a well-defined peak at $2\theta \approx 34.71°$ (JCPDS No. 36-1451), characteristic of the hexagonal wurtzite structure. Ashour et al. [48] found that at 1 wt.% Al doping, the peak remains close to its original position ($2\theta \approx 34.65°$), with a slight broadening, indicating minor structural modifications. However, as the Al concentration increases to 3 wt.% and 5 wt.%, a significant shift toward lower angles ($2\theta \approx 32.01°$ and 32.09°, respectively) is observed (Table 1), indicating an expansion of the lattice along the a-axis. Alrefaee et al. [50] confirmed that this shift is consistent with the increase in lattice parameters, suggesting lattice expansion. Additionally, Hallani et al. [51] reported that this shift is accompanied by the emergence of a stronger (100) peak, confirming a transition in preferred growth orientation from (002) to (100), as previously noted in Fig. 3(b).

The shift in peak position and broadening at higher Al concentrations suggest increased lattice strain and defect formation due to the substitution of Zn^{2+} (0.74 Å) by smaller Al^{3+} (0.53 Å). Al-Shehri et al. [18] found that this incorporation induces compressive strain in the ZnO structure, leading to altered growth dynamics and reduced crystallinity. The sharper peak at 5 wt.% Al doping suggests some degree of lattice relaxation, possibly due to the formation of Al-rich secondary phases or grain boundary segregation.

The lattice constants of ZnO thin films change with Sn and Al doping due to ionic size differences and strain effects. Sn doping slightly increases the c-axis parameter at 1 wt.% but induces lattice relaxation at higher concentrations due to defect formation. Al doping introduces compressive strain, reducing the c-axis and expanding the a-axis, shifting growth orientation from (002) to (100).

Kumar et al. [52] confirmed that the peak position of the (002) plane shifts slightly to lower angles at 1 wt.% Sn doping (from 34.71° to 34.48°) but moves back at higher concentrations due to lattice relaxation. Similarly, Afifah et al. [53] noted that Al doping shifts the (002) peak to lower angles, with a significant shift observed at 3 wt.% and 5 wt.% (from 34.71° to ~32.01°). These variations

[DOI: 10.22068/ijmse.4142]

affect crystallinity and microstrain, influencing the film's structural integrity (Table 1).

Fig. 5(a) and (b) illustrate the influence of Sn and Al doping on the crystallite size and microstrain of ZnO thin films. At 1 wt.% Sn doping, the crystallite size reaches 37.98 nm with reduced microstrain (9.14×10-4), indicating improved crystallinity [46]. At 3 wt.% Sn, the (002) peak intensity increases, suggesting that the incorporation of Sn into the ZnO lattice becomes more homogeneous, partially reducing lattice distortion and improving crystallinity. However, despite this increase in intensity, the crystallite size decreases, and strain increases (Table 1).

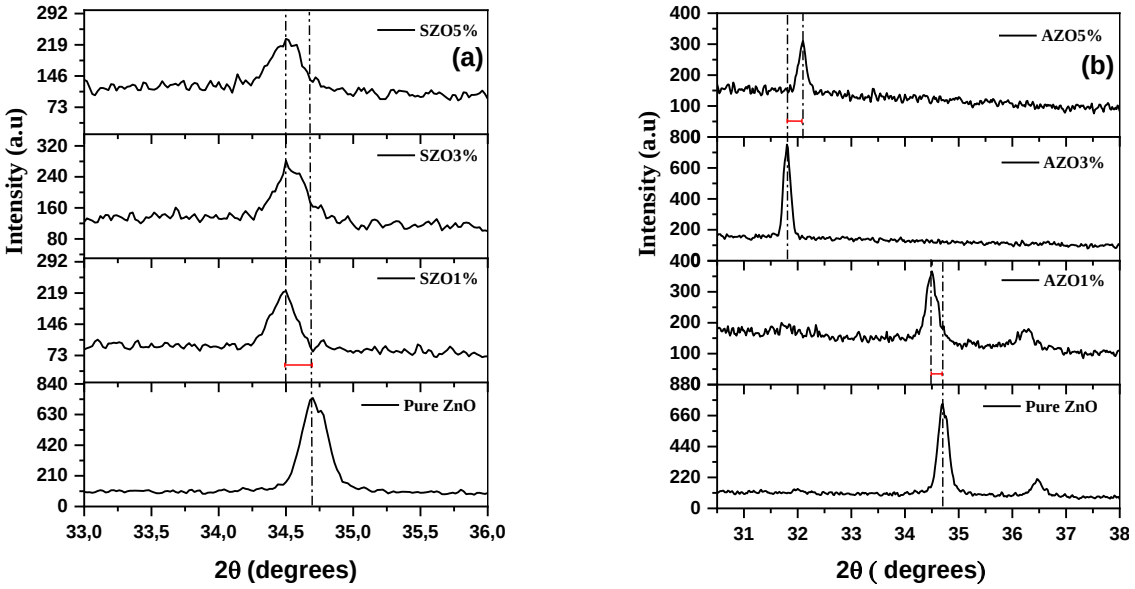

Fig. 4. Enlarged XRD patterns focusing on the (002) diffraction peak for a) Sn-doped ZnO and b) Al-doped ZnO films, highlighting shifts due to doping

Table 1. Structural parameters of ZnO thin films doped with Sn and Al, including lattice constants, crystallite size, microstrain, and peak position shifts from XRD analysis

Samples	Sn/Al (wt.%)	2θ (°)	FWHM (°)	D (nm)	ε×10^{-4}	d_{002} (Å)	d_{100} (Å)	c (Å)	a (Å)
Pure ZnO	**0**	34.712	0.2262	36.82	9.42	2.584		5.168	3.226
SZO	**1**	34.477	0.2193	37.98	9.14	2.584	/	5.168	3.226
	3	34.531	0.2449	33.98	10.21	2.597		5.194	3.242
	5	34.497	0.2499	33.31	10.41	2.599		5.199	3.245
AZO	**1**	34.650	0.2315	35.97	9.64	2.588	/	5.177	3.231
	3	32.012	0.2132	38.79	8.94	/	2.795	5.171	3.228
	5	32.087	0.1701	48.63	7.13		2.789	5.160	3.221

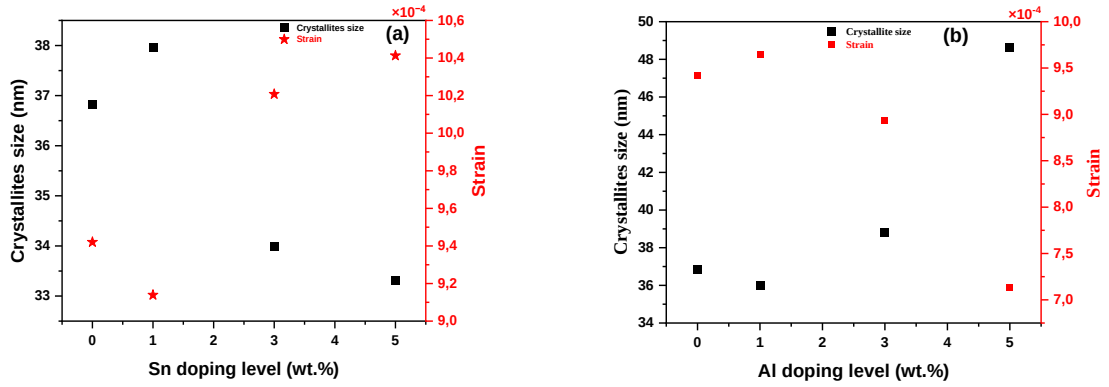

Fig. 5. Effect of a) Sn and b) Al doping concentrations on crystallite size and microstrain in ZnO thin films, calculated using Scherrer's equation

[DOI: 10.22068/ijmse.4142]

This is because at 3 wt.%, while the doping is more uniformly distributed, the increased concentration of Sn still leads to lattice strain, as the larger number of Sn^{4+} ions causes more defects and disruptions in the crystal structure. At higher doping levels (5 wt.% Sn), the strain becomes more pronounced, and the crystallite size decreases further, as the higher concentration of Sn^{4+} causes more structural distortions and defects. Alqaisi and Ghazai [54] reported that Sn doping affects the orientation and morphology of ZnO thin films, with excessive doping shifting the orientation from the (002) plane to other planes such as (101) and even leading to amorphous structures.

A similar trend is observed with Al doping, where 1 wt.% results in a moderate crystallite size (35.97 nm) and lower strain (9.64×10^{-4}), while excessive doping at 3 wt.% and 5 wt.% induces structural distortions, reducing crystallite size [55]. Bedia et al. [55] also found that Al-doped ZnO thin films exhibit a hexagonal wurtzite structure with a preferred orientation along the c-axis and high transparency in the visible range. These findings suggest that excessive dopant incorporation degrades crystallinity by increasing the density of defects.

The elemental composition analysis in Figs. 6(a) and 6(b) confirm the presence of Zn, O, and the respective dopants (Sn or Al), with increasing doping levels leading to a rise in Sn or Al content, while Zn and O decrease slightly. Munna et al. [56] reported that Sn substitutes Zn sites in the ZnO lattice, but at higher concentrations (>3 wt.%), possible SnO_2 phase formation may degrade crystallinity and charge transport. Similarly, Ahmed et al. [57] found that Al incorporation induces compressive strain due to the smaller ionic radius of Al^{3+}, affecting the film's structural integrity.

Fig. 6(c) and 6(d) illustrate that excessive Sn or Al doping can lead to phase segregation or secondary phase formation, modifying the film's morphology and electronic properties [58]. At 1 wt.% Sn or Al, doping enhances crystallinity and charge mobility, improving optoelectronic performance [56, 57]. However, Jongprateep et al. [59] found that higher concentrations (>3 wt.%) introduce defects, shifting orientation from (002) to (100) (in the case of Al) and increasing recombination centers, ultimately reducing photo-catalytic efficiency.

The SEM images and particle size distribution in Fig. 7 illustrate the morphological evolution of ZnO thin films with Sn doping. The pure ZnO film exhibits relatively uniform, well-defined grains with an average particle size of 279.43 nm, indicating high crystallinity and minimal defects.

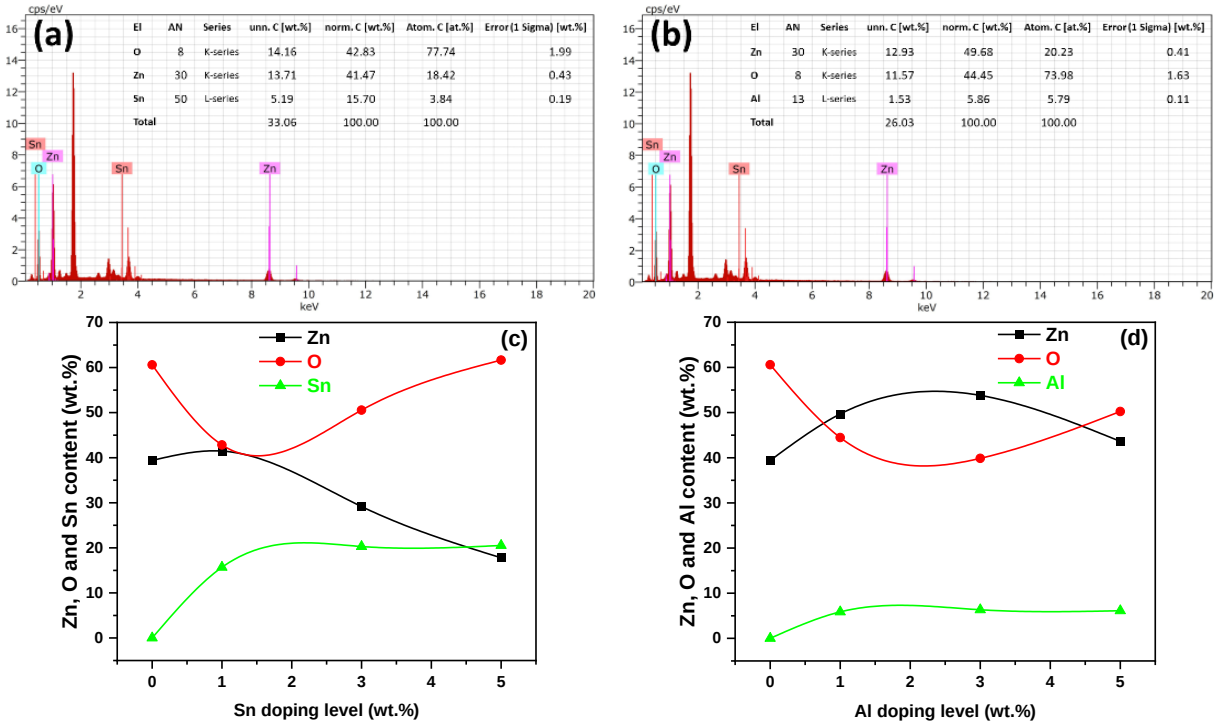

Fig. 6. Elemental composition analysis of ZnO thin films using energy-dispersive X-ray spectroscopy (EDX): a) ZnO:Sn (1 wt.%), b) ZnO:Al (1 wt.%), and c) comparative elemental composition of Sn-doped and d) Al-doped ZnO thin films at different doping concentrations

[DOI: 10.22068/ijmse.4142]

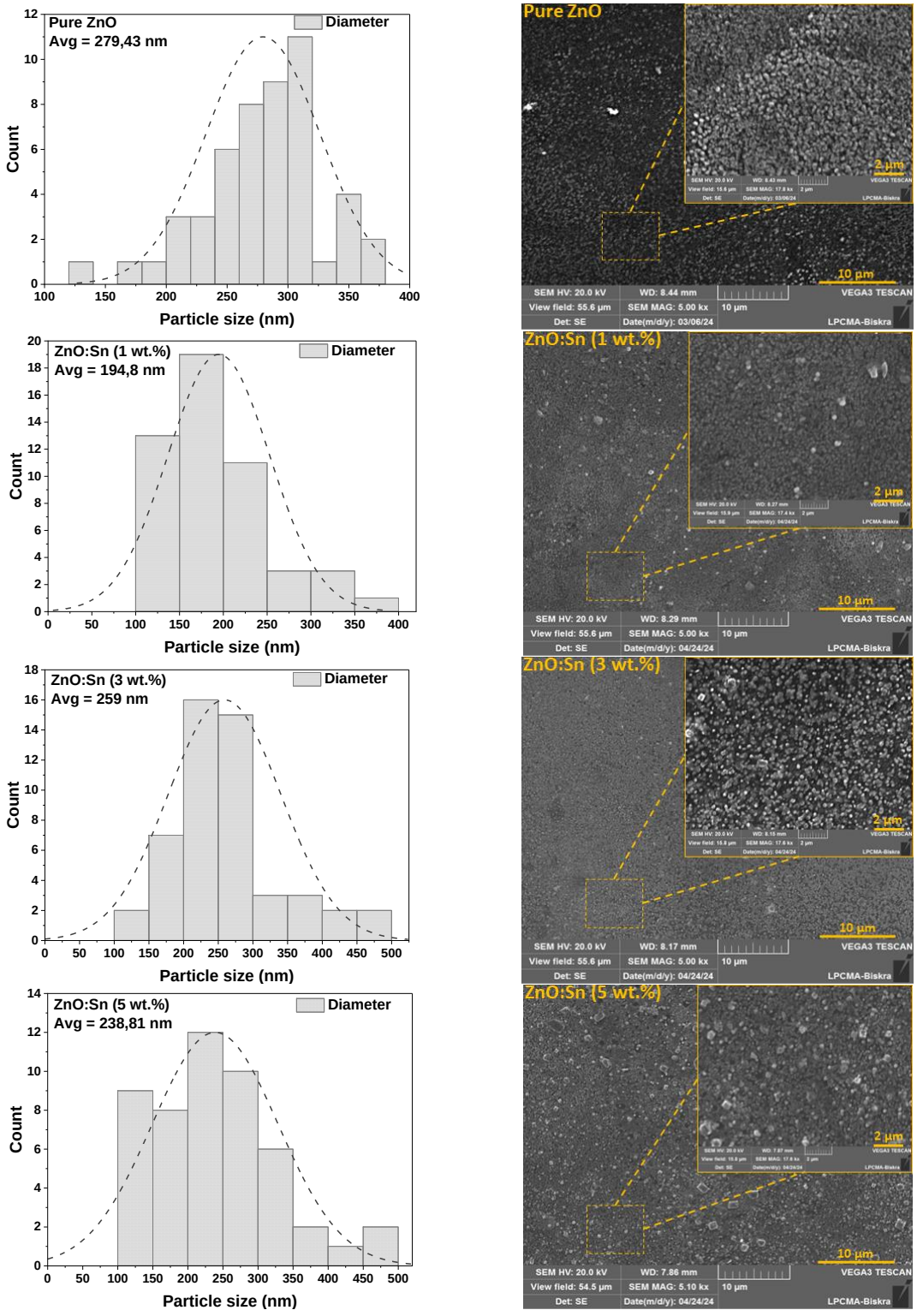

Fig. 7. SEM images and particle size distribution of pure ZnO and Sn-doped ZnO thin films at different doping concentrations, obtained from SEM analysis

At 1 wt.% Sn doping, the particle size decreases to 194.8 nm, and the SEM images reveal a denser microstructure with smaller, more compact grains, which supports the findings of Prabhu et al. [60], who found that Sn promotes nucleation, increasing the number of grain boundaries, which enhances surface area—a crucial factor for photocatalytic performance.

[DOI: 10.22068/ijmse.4142]

However, at 3 wt.% Sn doping, the particle size increases to 259 nm, accompanied by a more aggregated morphology, suggesting grain coalescence due to Sn-induced lattice strain [56]. At 5 wt.% Sn doping, the particle size decreases again to 238.81 nm, with SEM images revealing an irregular, rougher surface with increased porosity. Sharma et al. [49] noted that excessive Sn incorporation creates defects and disrupts uniform crystal growth, which aligns with the observed morphological changes. These variations in morphology influence light absorption and charge carrier dynamics. As Prabhu et al. [60] emphasized, smaller, well-distributed grains at 1 wt.% Sn doping provides an optimal balance between crystallinity and surface area, enhancing photocatalytic performance by improving light absorption and reducing electron-hole recombination.

The SEM images and particle size distribution in Fig. 8 illustrate the morphological evolution of ZnO thin films with Al doping. The ZnO:Al (1 wt.%) film exhibits the largest average particle size (341.5 nm), with well-defined, compact grains, suggesting that a small amount of Al promotes grain growth by reducing lattice defects. This finding aligns with studies indicating that Al incorporation enhances crystallinity and reduces defect density in ZnO films.

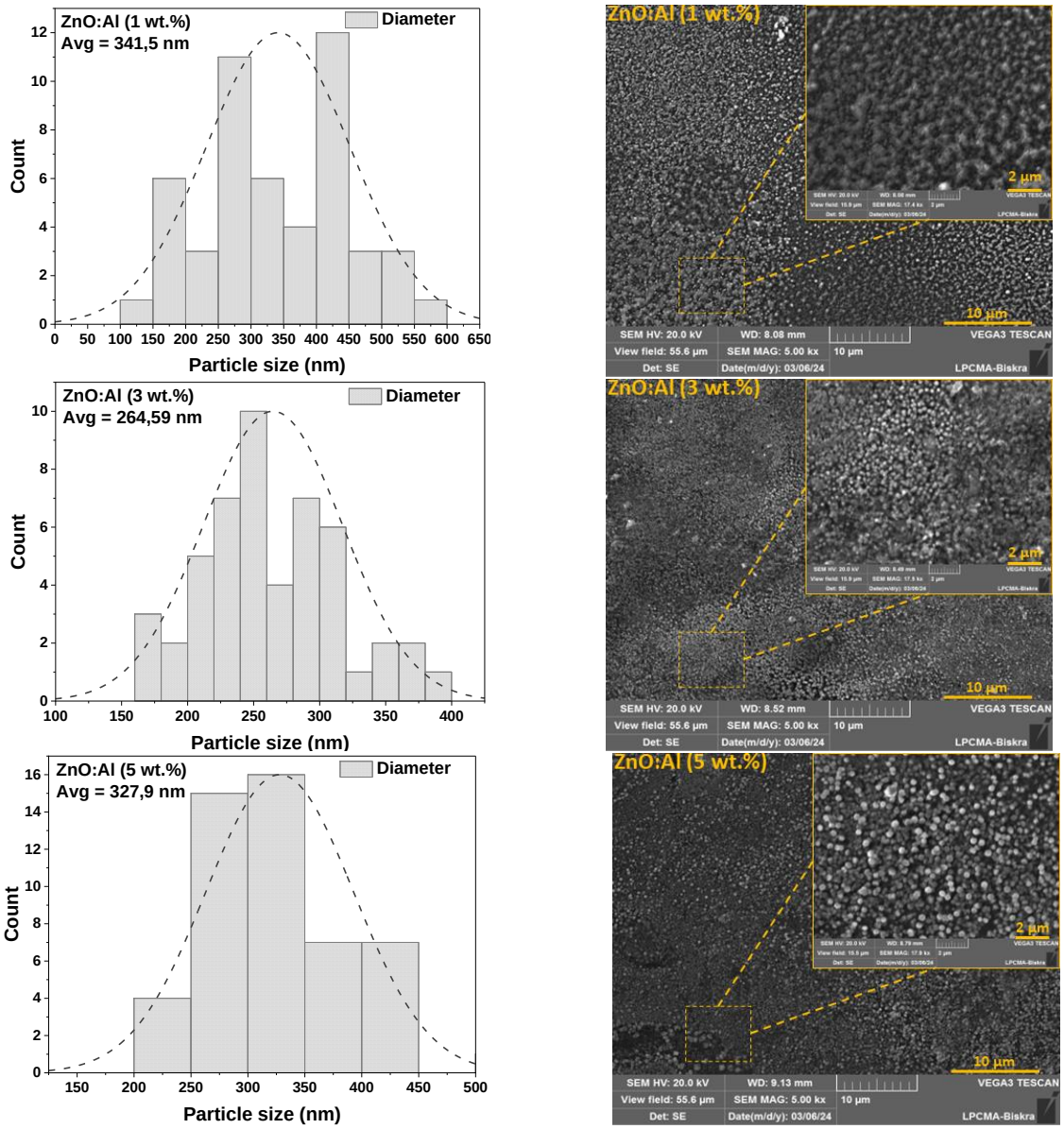

Fig. 8. SEM images Particle size distribution of Al-doped ZnO thin films at different doping concentrations, as determined from SEM analysis

[DOI: 10.22068/ijmse.4142]

However, at 3 wt.% Al doping, the particle size decreases significantly to 264.59 nm, and the SEM images show a more fragmented, less compact surface. Ahmed et al. [61] noted that excessive Al incorporation introduces lattice strain and defect sites, limiting grain coalescence, which explains the observed reduction in particle size. Similarly, Saxena et al. [62] confirmed that higher Al doping can increase defect density, affecting film morphology. At 5 wt.% Al doping, the particle size increases again to 327.9 nm, with SEM images revealing a rougher, more porous surface. Al-Shehri et al. [18] stated that higher Al concentrations may lead to Al atom segregation at grain boundaries, causing localized stress relaxation and partial grain regrowth, which is consistent with the observed structural changes.

These modifications influence charge carrier mobility and light absorption. As Ahmed et al. [61] and Afifah et al. [53] reported, moderate Al doping can enhance photocatalytic performance by increasing active surface area. However, excessive doping introduces recombination centers, negatively affecting efficiency, as highlighted by Al-Hardan et al. [63] and Tonka et al. [64].

Fig. 9 presents the optical transmittance spectra of ZnO thin films doped with Sn (Fig. 9a) and Al (Fig. 9b). Pure ZnO exhibits high transmittance (~80-90%) in the visible range, reflecting good crystallinity and minimal defect scattering. For Sn-doped ZnO (SZO), Marotti et al. [65] observed that transmittance slightly decreases at 1 wt.% due to enhanced free carrier absorption, resulting from increased carrier concentration. At 3 wt.%, a more pronounced drop occurs, likely caused by increased microstrain and defect density, which scatter light and reduce optical clarity. At 5 wt.%, a further reduction suggests the formation of Sn-related secondary phases, introducing additional light scattering and optical losses.

Similarly, for Al-doped ZnO (AZO), Petrov et al. [66] and Salim [13] reported that 1 wt.% Al doping maintains comparable transmittance to pure ZnO, indicating minimal impact on optical properties at low doping levels. However, at 3 wt.%, a slight decrease in transmittance is observed due to higher carrier concentration and light scattering, as confirmed by Ahmed et al. [61] and Afifah et al. [53]. At 5 wt.%, the transmittance drops further, likely due to defect states and structural distortions introduced by excessive Al incorporation, which is consistent with the findings of Mishra et al. [67] and Tonka et al. [64]. The overall decrease in transmittance with increasing doping levels can be attributed to enhanced free carrier absorption, defect formation, and bandgap narrowing [53, 61, 65]. Since moderate doping levels enhance light absorption while maintaining reasonable crystallinity, ZnO:Sn and ZnO:Al films can be optimized for visible-light-driven photocatalytic degradation of organic pollutants.

Fig. 10 illustrates the Tauc plots used to determine the optical bandgap energy (Eg) of ZnO thin films doped with Sn (Fig. 10a) and Al (Fig. 10b). Pure ZnO exhibits a bandgap of approximately 3.254 eV, characteristic of well-crystallized ZnO. For Sn-doped ZnO (SZO), Babalola et al. [44] and Sharma et al. [49] reported that the bandgap initially decreases to 3.142 eV at 1 wt.% due to the introduction of localized electronic states within the bandgap caused by Sn incorporation. At 3 wt.%, the bandgap slightly increases to 3.249 eV, possibly due to lattice relaxation or phase segregation effects.

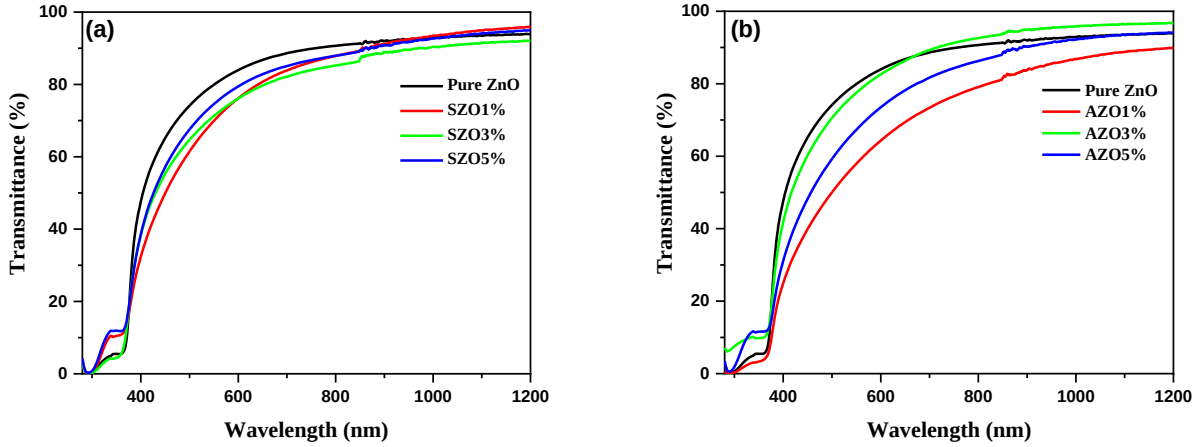

Fig. 9. Optical transmittance spectra of ZnO thin films doped with a) Sn and b) Al

[DOI: 10.22068/ijmse.4142]

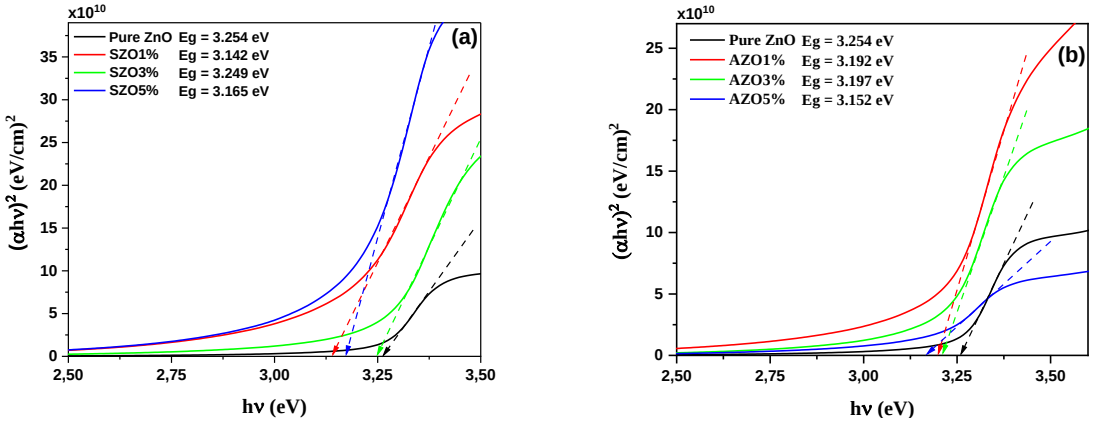

Fig. 10. Tauc plot for bandgap determination of ZnO thin films doped with a) Sn and b) Al, showing variations in optical bandgap energy with doping concentration

However, at 5 wt.%, the bandgap narrows again to 3.165 eV, indicating increased defect levels and sub-bandgap absorption, which is consistent with the findings of Boufelgha et al. [47].

Similarly, for Al-doped ZnO (AZO), Petrov et al. [66] and Salim [13] observed that the bandgap decreases at 1 wt.% (3.192 eV) due to enhanced carrier concentration and impurity states. At 3 wt.% and 5 wt.%, the bandgap remains relatively stable (~3.152 eV), suggesting that excessive Al doping saturates defect formation with minimal additional impact on band structure, as noted by Bouacheria et al. [68]. The observed bandgap narrowing with Sn and Al doping can be explained by the Burstein-Moss shift at low doping levels, which increases the bandgap due to higher carrier concentration [57, 69]. At higher doping concentrations, defect-related bandgap reduction dominates, enhancing visible-light absorption and making ZnO:Sn and ZnO:Al films suitable for photocatalytic applications, such as the degradation of organic pollutants under solar irradiation [45, 47].

Fig. 11 illustrates the variation of Urbach energy (Eu), which quantifies the structural disorder in ZnO thin films. Pure ZnO exhibits the lowest Eu, reflecting its well-ordered crystalline structure with minimal defect states. For Sn-doped ZnO (SZO), Eu increases with doping concentration, indicating the introduction of disorder and defect states within the material. The highest disorder is observed at 5 wt.% Sn, where excessive doping leads to significant lattice strain and localized defect states. This increased disorder enhances sub-bandgap absorption, affecting the material's optical properties.

Similarly, for Al-doped ZnO (AZO), Eu follows a rising trend with increasing Al content [13]. At 5 wt.% Al, the disorder reaches its peak, suggesting that excessive doping disrupts the crystal structure and increases localized defects. The widening of the optical bandgap at moderate doping levels, coupled with increased disorder at higher concentrations, influences the material's photocatalytic performance.

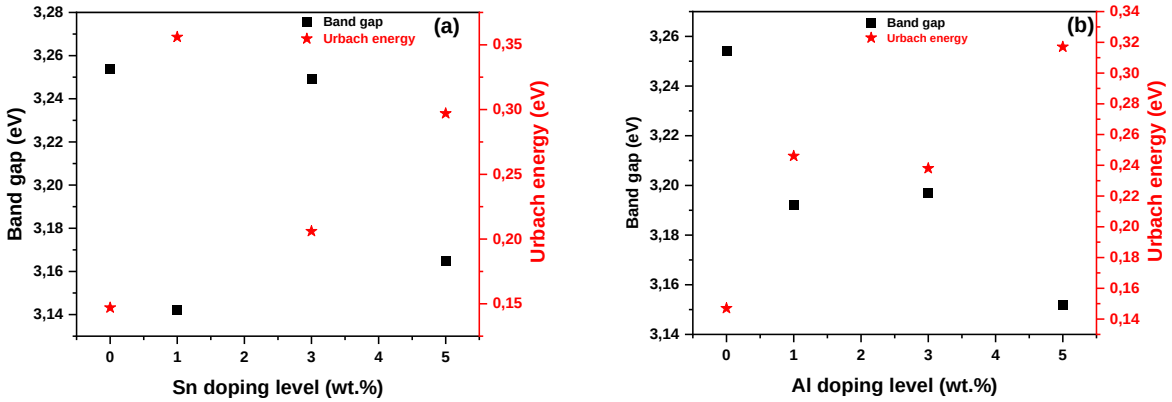

Fig. 11. Variation of bandgap energy and Urbach energy as a function of a) Sn and b) Al doping concentrations in ZnO thin films

[DOI: 10.22068/ijmse.4142]

The combined effects of bandgap narrowing (Fig. 10) and rising Urbach energy (Fig. 11(a) and (b)) indicate that moderate doping levels optimize visible-light absorption. As a result, ZnO:Sn and ZnO:Al films exhibit enhanced photocatalytic activity, making them effective materials for the solar-driven degradation of organic pollutants.

Fig. 12a to 12c present the UV-Vis absorption spectra of methylene blue (MB) degradation under solar irradiation for pure ZnO, Sn-doped ZnO (1 wt.%), and Al-doped ZnO (1 wt.%) thin films. The gradual decline in the MB absorption peak at ~664 nm confirms the photodegradation of the dye [31]. However, the persistence of absorbance in the UV region (below 400 nm) suggests that the process is primarily decolorization rather than complete mineralization. This suggests that intermediate organic species remain in the solution, preventing full oxidation of MB into CO_2, H_2O, and inorganic byproducts. Decolorization results from the breakdown of MB's chromophore structure, making the solution appear colorless while still containing organic residues. Among the tested films, pure ZnO exhibits the highest efficiency in reducing overall absorbance, achieving significant MB degradation due to its strong electron-hole separation and effective generation of reactive oxygen species. In contrast, Sn- and Al-doped ZnO films demonstrate comparatively lower photocatalytic performance. This reduction in efficiency is likely due to the formation of charge recombination centers introduced by excess dopants, which hinder the separation of photogenerated charge carriers essential for efficient photocatalysis [70, 71].

Fig. 12d further illustrates the degradation efficiency of methylene blue (MB) by showing the progressive decrease in MB concentration over time for all thin films. The superior photocatalytic performance of pure ZnO can be attributed to its high crystallinity, low defect density, and enhanced charge separation, as discussed in the manuscript. In contrast, Sn and Al doping introduce structural defects and lattice distortions, which act as charge recombination centers, reducing the number of photogenerated charge carriers available for redox reactions. The MB degradation mechanism follows a typical semiconductor photocatalytic pathway. (i) ZnO absorbs photons, generating electron-hole pairs:

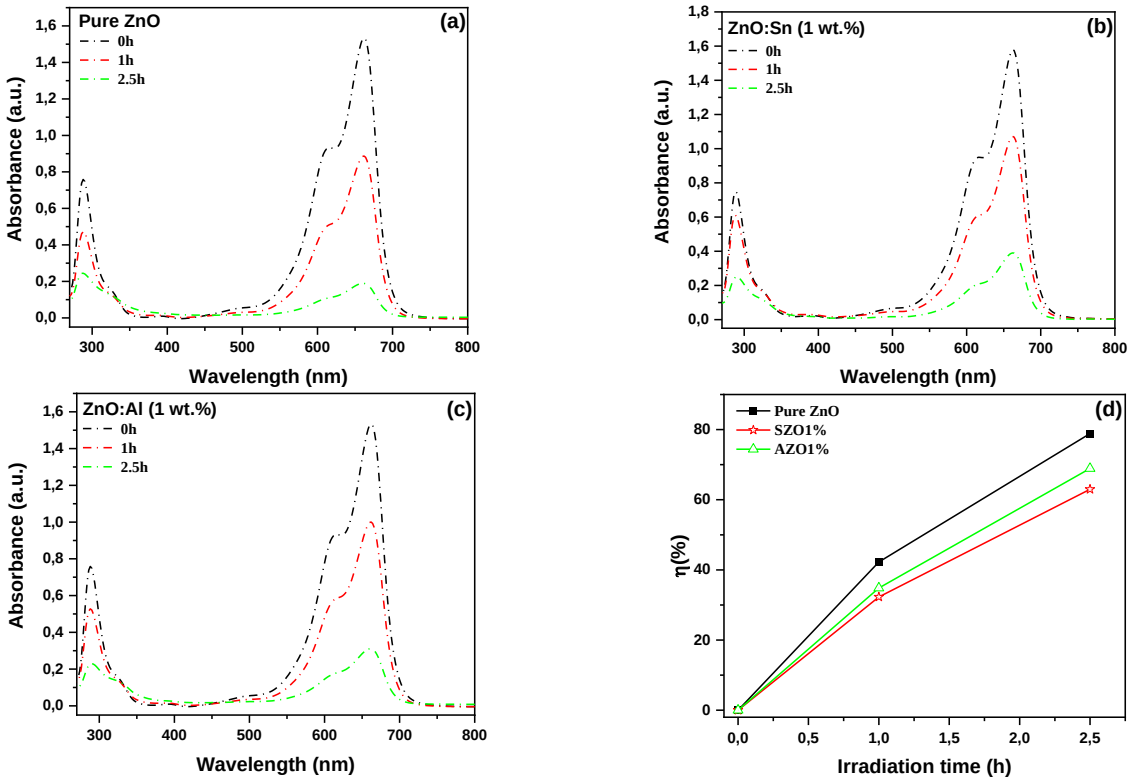

Fig. 12. a–c) UV-Vis absorption spectra of methylene blue (MB) degradation over time under solar irradiation for a) pure ZnO, b) Sn-doped ZnO (1 wt.%), and c) Al-doped ZnO (1 wt.%) thin films. d) Photocatalytic degradation efficiency of MB as a function of irradiation time for pure and doped ZnO thin films

[DOI: 10.22068/ijmse.4142]

$ZnO + hv \rightarrow e^- + h^+$ (9)

When ZnO is exposed to solar irradiation, electrons (e^-) are excited from the valence band to the conduction band, creating holes (h^+) in the valence band [72, 73]. (ii) Holes react with water to generate hydroxyl radicals:

$h^+ + H_2O \rightarrow \bullet OH^- + H^+$ (10)

The photogenerated holes interact with water molecules, forming highly reactive hydroxyl radicals (•OH), which are powerful oxidizing agents that degrade organic pollutants [72]. (iii) Electrons reduce oxygen to form superoxide radicals:

$e^- + O_2 \rightarrow \bullet O_2^-$ (11)

The conduction band electrons react with dissolved oxygen to form superoxide anions ($\bullet O_2^-$), which further contribute to the oxidation and degradation of MB. (iv) Hydroxyl and superoxide radicals attack MB molecules, breaking them down [1]:

$$\begin{pmatrix} \bullet OH^- + MB \rightarrow \text{Colorless organic intermediates, (Decolorization)} \\ \text{Colorless organic intermediates} + \bullet OH^- \rightarrow CO_2 + H_2O + NO_3^-, \text{(Mineralization)} \end{pmatrix} \quad (12)$$

These reactive oxygen species (ROS) continuously attack MB, breaking down its structure into smaller organic fragments, leading to decolorization. If the reaction progresses further, the radicals continue oxidizing the organic fragments, ultimately converting MB into carbon dioxide (CO_2), water (H_2O), and inorganic ions like nitrates (NO_3^-), achieving complete mineralization. Findings suggest that ZnO's superior performance arises from its higher crystallinity, optimal charge carrier mobility, and better light absorption properties, all of which enhance the generation of reactive oxygen species. The Sn- and Al-doped ZnO films, despite increasing electrical conductivity, introduce excess defects that promote charge recombination, thereby lowering photocatalytic efficiency.

Fig. 13a illustrates the first-order kinetic plots for MB degradation using pure ZnO, Sn-doped ZnO (SZO1%), and Al-doped ZnO (AZO1%) thin films. The linearity of these plots confirms that MB degradation follows a pseudo-first-order kinetic model, with the slope corresponding to the apparent reaction rate constant (k_{app}). Among the samples, pure ZnO demonstrates the highest degradation rate (k_{app}= 0.8552 h^{-1}), attributed to its superior crystallinity, minimal defect density, and efficient charge carrier separation, which collectively minimize recombination losses.

In comparison, the SZO1% and AZO1% films exhibit lower degradation rates, with k_{app}= 0.5569 h^{-1} and k_{app}= 0.6483 h^{-1}, respectively. The reduction in efficiency is likely due to structural distortions and the formation of recombination centers induced by doping, which hinder charge separation and accelerate recombination [47, 74].

Fig. 13b quantifies these trends by displaying the apparent reaction rate constants (k_{app}), confirming that pure ZnO exhibits the highest photocatalytic efficiency, followed by AZO1% and then SZO1%. The regression coefficient (R^2) values for all samples are close to 1 (R^2= 0.97572 for pure ZnO, R^2= 0.97579 for SZO1%, and R^2= 0.97791 for AZO1%), indicating an excellent fit to the pseudo-first-order kinetic model and validating the predictability of the degradation process. However, the lower k_{app} values for doped ZnO films suggest that charge recombination is more pronounced in these samples, thereby reducing overall photo-catalytic efficiency. These findings emphasize that while doping modifies the electrical and optical properties of ZnO, excessive doping (>1 wt.%) increases the defect density, alters the crystal orientation, and ultimately diminishes the photo-catalytic performance.

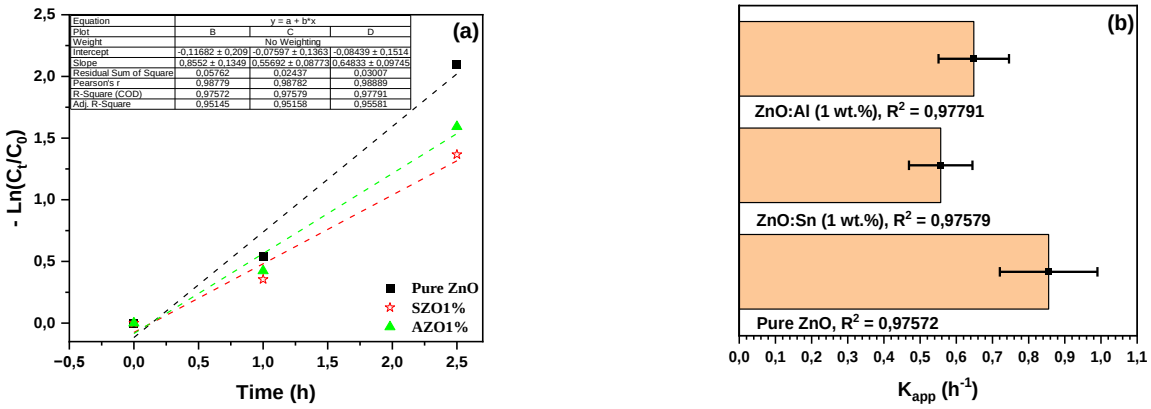

Fig. 13. a) First-order kinetic plots of MB degradation using pure ZnO, Sn-doped ZnO, and Al-doped ZnO thin films. b) Apparent reaction rate constants (k_{app}) for different photocatalysts.

[DOI: 10.22068/ijmse.4142]

Optimizing the doping concentration while preserving ZnO's structural integrity is essential for maximizing its photocatalytic activity.

Fig. 14 presents the adsorption isotherms of methylene blue (MB) on ZnO-based thin films, including pure ZnO, Sn-doped ZnO (SZO), and Al-doped ZnO (AZO), as predicted by the Langmuir adsorption model. This model assumes monolayer adsorption on a homogeneous surface with a finite number of identical adsorption sites. The experimental data for ZnO, SZO, and AZO were fitted using the linearized Langmuir equation:

$$\frac{C_e}{q_e} = \frac{1}{q_{max}} . C_e + \frac{1}{K_L q_{max}} \quad (13)$$

where q_e (mg/g) represents the equilibrium adsorption capacity, q_{max} (mg/g) is the maximum adsorption capacity, C_e (mg/L) is the equilibrium concentration, and K_L (L/mg) is the Langmuir constant related to adsorption affinity.

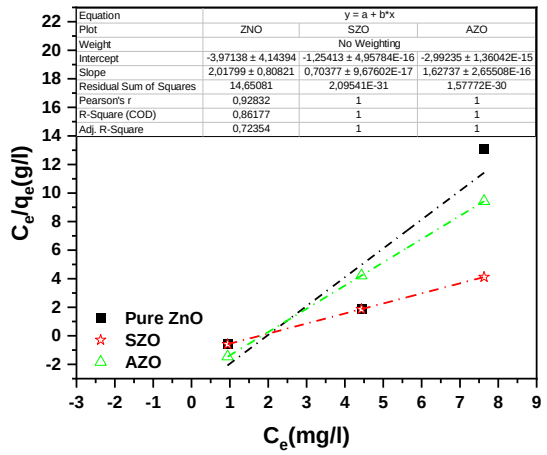

Fig. 14. Linearized Langmuir adsorption isotherms for Methylene Blue on ZnO-based thin films

The fitting results, summarized in Table 2, indicate that SZO exhibits the highest adsorption capacity, with q_{max}= 1.422 mg/g with an excellent linear fit (R^2= 1.000), suggesting strong MB adsorption onto its surface. This implies that Sn doping enhances the adsorption sites or affinity for MB molecules [75]. Similarly, AZO also follows the Langmuir model well (R^2= 1.000) but demonstrates a lower adsorption capacity (q_{max}= 0.617 mg/g), likely due to the impact of Al doping on surface reactivity and charge distribution, which affects the overall adsorption behavior [75]. In contrast, pure ZnO shows a moderate fit to the Langmuir model (R^2= 0.861) with a significantly lower adsorption capacity (q_{max}= 0.495 mg/g), indicating weaker dye-surface interactions [76].

The negative K_L values observed for all samples may suggest experimental uncertainties or deviations from ideal Langmuir behavior, possibly due to multilayer adsorption effects or electrostatic interactions between MB molecules and doped ZnO surfaces [77, 78]. These findings highlight that while doping enhances the adsorption capacity of ZnO, Sn doping is particularly effective in improving dye uptake, making SZO a promising candidate for MB removal in wastewater treatment applications.

These findings highlight the significant impact of Sn and Al doping on the structural, optical, and photocatalytic properties of ZnO thin films. While moderate doping (1 wt.%) enhances crystallinity and adsorption capacity, excessive doping (>3 wt.%) introduces defects that reduce photocatalytic efficiency by increasing charge recombination. Pure ZnO demonstrates the highest photocatalytic activity, while Sn-doped ZnO exhibits superior MB adsorption capacity. Optimizing doping concentrations and deposition conditions is crucial for balancing structural integrity, charge transport, and surface reactivity to enhance ZnO-based materials for environmental and photocatalytic applications.

4. CONCLUSIONS

The findings of this study highlight the critical influence of Sn and Al doping on the structural, optical, and photocatalytic properties of ZnO thin films synthesized via a cost-effective pneumatic spray technique. Optimal doping concentrations (1 wt.% Sn and 5 wt.% Al) enhanced crystallinity, with maximum crystallite sizes of 37.98 nm and 48.63 nm, respectively, while excessive doping (>3 wt.%) increased microstrain (10.41×10^{-4} for Sn and 7.13×10^{-4} for Al), leading to structural defects.

Table 2. Langmuir isotherm parameters for Methylene Blue adsorption on ZnO-based thin films

Absorbent	Equation (y= f(x))	R^2	q_{max} (mg/g)	K_L (L/mg)	S_{MB} (10^{-20}km^2/kg)
Pure ZnO	2.017x-3.97	0.861	0.495	-0.508	1.571
SZO	0.703x-1.25	1	1.422	-0.562	4.514
AZO	1.620x-2.99	1	0.617	-0.542	1.958

[DOI: 10.22068/ijmse.4142]

The bandgap energy decreased from 3.254 eV (pure ZnO) to 3.142 eV (1 wt.% Sn) and 3.152 eV (5 wt.% Al), accompanied by an increase in Urbach energy to 0.34 eV for highly doped films, indicating the presence of enhanced defect states. The highest optical transmittance (86%) was observed for 3 wt.% Al-doped ZnO, confirming its potential for optoelectronic applications. Photocatalytic analysis demonstrated that pure ZnO exhibited the best performance, achieving 85% methylene blue degradation under solar irradiation, while Langmuir adsorption modelling showed that Sn-doped ZnO had the highest adsorption capacity (1.422 mg/g), followed by Al-doped ZnO (0.617 mg/g) and pure ZnO (0.495 mg/g). Despite these promising results, limitations such as defect formation at higher doping levels, the absence of co-doping strategies, and the need for long-term stability assessments remain challenges. Additionally, one limitation of the present work is the absence of photoluminescence (PL) characterization, which could provide direct insight into recombination and defect states. Future research should focus on refining doping concentrations, optimizing deposition conditions, and exploring alternative dopants to further enhance ZnO-based thin films for sustainable optoelectronic and environmental applications.

ACKNOWLEDGMENTS

The authors would like to thank the Algerian Directorate General for Scientific Research and Technological Development -DGRSDT for financial assistance.

REFERENCES

[1] Nezzal, H., Rahmane, S., Temam, E. G., Al-Abri, M., Kyaw, H. H., Gasmi, B., Althamthami, M., Ben Temam, H., Hu, J., "Photo-deposition of AgO thin films on TiO_2 substrate for (P-N) hetero-junction applications: Considering the degree of contamination". J. Alloys. Compd., 2025, 1010, 177331.

[2] Wu, Y., Zhang, D. B., Zhao, Z., Pei, J., Zhang, B. P., "Enhanced thermoelectric properties of ZnO: C doping and band gap tuning". J. Eur. Ceram. Soc., 2021, 41, 1324–1331.

[3] Cui, W., Chen, P., Chen, L., al, Hasibur Rahman, K., Kumar Kar, A., Chen, K.-C., Mehtab, A., Ahmed, J., Alshehri, S. M., Kumar, R., Dosanjh, H. S., "A mini-review on rare earth metal doped ZnO nano-materials for photocatalytic remediation of waste water". J. Phys. Conf. Ser., 2022, 2267, 012139.

[4] Mokrani, N., Temam, E. G., Ben Temam, H., Barkat, H., Althamthami, M., "Enhancing water purification with light-activated strontium-doped ZnO thin films". Advances in Natural Sciences: Nanoscience and Nanotechnology, 2025, 16, 015012.

[5] Derbali, L., "Electrical and Optoelectronic Properties Enhancement of n-ZnO/p-GaAs Heterojunction Solar Cells via an Optimized Design for Higher Efficiency". Materials, 2022, 15, 6268.

[6] Saleem, S., Jameel, M. H., Rehman, A., Tahir, M. B., Irshad, M. I., Jiang, Z. Y., Malik, R. Q., Hussain, A. A., Rehman, A. U., Jabbar, A. H., Alzahrani, A. Y., Salem, M. A., Hessien, M. M., "Evaluation of structural, morphological, optical, and electrical properties of zinc oxide semi-conductor nanoparticles with microwave plasma treatment for electronic device applications". Journal of Materials Research and Technology, 2022, 19, 2126–2134.

[7] Barkat, H., Guettaf Temam, E., Ben Temam, H., Mokrani, N., Rahmane, S., Althamthami, M., "Thickness-dependent photocatalytic performance and wettability of barium-doped ZnO thin films synthesized via SILAR technique". Transition Metal Chemistry, 2025, 50, 431–450.

[8] Yousra, K., Guettaf Temam, E., Saâd, R., Barkat, H., "Effect of film thickness on the electrical and the photocatalytic properties of ZnO nanorods grown by SILAR technique". Phys. Scr., 2023, 12, 125954.

[9] Nadikatla, S. K., Chintada, V. B., Gurugubelli, T. R., Koutavarapu, R., "Review of Recent Developments in the Fabrication of ZnO/CdS Heterostructure Photocatalysts for Degradation of Organic Pollutants and Hydrogen Production". Molecules, 2023, Vol. 28, Page 4277, 2023, 28, 4277.

[10] Mishra, K., Devi, N., Siwal, S. S., Gupta, V. K., Thakur, V. K., "Hybrid Semi-conductor Photocatalyst Nanomaterials for Energy and Environmental Applications:

[DOI: 10.22068/ijmse.4142]

Fundamentals, Designing, and Prospects". Adv. Sustain. Syst., 2023, 7, 2300095.
[11] Banerjee, D., Kumar Kar, A., "Structural strategy to enhance the quantum and photocatalytic efficiency of ZnO quantum dots by incorporation of interface states". J. Photochem. Photobiol. A. Chem., 2023, 437, 114500.
[12] Hezam, A., Drmosh, Q. A., Ponnamma, D., Bajiri, M. A., Qamar, M., Namratha, K., Zare, M., Nayan, M. B., Onaizi, S. A., Byrappa, K., "Strategies to Enhance ZnO Photocatalyst's Performance for Water Treatment: A Comprehensive Review". The Chemical Record, 2022, 22, e202100299.
[13] SALIM, K., "Study of the Influence of Doping on the Structural, Optical and Electrical Properties of zinc oxide thin Films Produced by by Spray Pyrolysis for Solar Cell Applications". Algerian Journal of Renewable Energy and Sustainable Development, 2023, 5, 48–55.
[14] Koskinen, T., Raju, R., Tittonen, I., Kauppinen, C., "Grass-like alumina enhances transmittance and electrical conductivity of atomic layer deposited Al-doped ZnO f or thermoelectric and TCO applications". Appl. Phys. Lett., 2023, 123, 011902.
[15] Mokrani, N., Guettaf Temam, E., Barkat, H., Ben Temam, H., Rahmane, S., Althamthami, M., "Boosting photocatalytic stability: hydrophilic Sr-doped ZnO thin films prepared via the SILAR method for enhanced performance over multiple cycles". Phys. Scr., 2024, 99, 0959a4.
[16] Barkat, H., Temam, E. G., Ben Temam, H., Mokrani, N., Rahmane, S., Althamthami, M., "Enhancing Sunlight-Driven Photo-catalysis: High Transparency and Hydrophilic Advancements in Ba-Doped ZnO Thin Films". J. Mater. Eng. Perform., 2024, 34, 12555–12568.
[17] Starowicz, Z., Zięba, A., Ostapko, J., Wlazło, M., Kołodziej, G., Jakub Szczerba, M., Putynkowski, G., Piotr Socha, R., "Synthesis and characterization of Al-doped ZnO and Al/F co-doped ZnO thin films prepared by atomic layer deposition". Materials Science and Engineering: B, 2023, 292, 116405.
[18] Al-Shehri, S., Alshehri, S., Ali, H. E., Alassafi, J. E., Alzahrani, A. O. M., Aida, M. S., "Al Doping Influence on the Properties of Sol–Gel Synthetized ZnO Nanoparticles". physica status solidi (a), 2023, 220, 2300272.
[19] Stroescu, H., Nicolescu, M., Mitrea, D., Tenea, E., Atkinson, I., Anastasescu, M., Calderon-Moreno, J. M., Gartner, M., "Effect of Al Incorporation on the Structural and Optical Properties of Sol–Gel AZO Thin Films". Materials, 2023, 16, 3329.
[20] Hossain, M. I., Mansour, S., "A critical overview of thin films coating technologies for energy applications". Cogent. Eng., 2023, 10, 2179467.
[21] Vázquez, V., Diana, E., Luna, L., José, A., Abundiz, C., Noemí., Juarez, D., Gabriel., "Synthesis and characterization of Zinc Oxide thin films deposited by Spray Pyrolysis technique for possible applications in solar cells". Journal Renewable Energy, 2022, 6, 8-14.
[22] Mazur, M., Obstarczyk, A., Posadowski, W., Domaradzki, J., Kiełczawa, S., Wiatrowski, A., Wojcieszak, D., Kalisz, M., Grobelny, M., Szmidt, J., "Investigation of the Microstructure, Optical, Electrical and Nanomechanical Properties of ZnOx Thin Films Deposited by Magnetron Sputtering". Materials, 2022, 15, 6551.
[23] Khiari, M., Gilliot, M., Lejeune, M., Lazar, F., Hadjadj, A., "Preparation of Very Thin Zinc Oxide Films by Liquid Deposition Process: Review of Key Processing Parameters". Coatings, 2022, 12, 65.
[24] Miasoiedova, A., Minska, N., Shevchenko, R., Azarenko, O., Lukashenko, V., Kyrychenko, O., Zemlianskyi, O., Trefilova, L., Kamyshentsev, G., Melezhyk, R., "Improving the manufacturing technology of sensing gas sensors based on zinc oxide by using the method of magnetron sputtering on direct current". Eastern-European Journal of Enterprise Technologies, 2023, 2, 31–37.
[25] Gordillo, G., Pena, J. C., "Development of system to grow ZnO films by plasma assisted reactive evaporation with improved thickness homogeneity for using in solar cells". Journal of Materials Research and Technology, 2022, 19, 1191–1202.
[26] Shkir, M., Khan, M. T., Khan, A., "Impact of Mo doping on photo-sensing properties of ZnO thin films for advanced photo-

[DOI: 10.22068/ijmse.4142]

detection applications". J. Alloys. Compd., 2024, 985, 174009.
[27] Mahroug, A., Mahroug, I., Berra, S., Hamrit, S., Guelil, A., Zoukel, A., Ullah, S., "Optical, Photocurrent, Electrical, Structural, and Morphological Properties of Magnetron Sputtered Pure and Iron-Doped Zinc Oxide Thin Films". ECS Journal of Solid State Science and Technology, 2023, 12, 046006.
[28] Wang, X., Zhong, Y., Pu, H., Liu, Y., Wang, W., Ma, J., "Structural and photoelectric properties of Sn-doped ZnO thin film with the co-sputtering method". J. Phys. Conf. Ser., 2022, 2370, 012031.
[29] Ahmad, M., Khan, Z., Rehman, M. M. U., Ali, A., Aslam, S., "A Study of Aluminum Doped ZnO Thin Films Developed via a Hybrid Method Involving Sputter Deposition and Wet Chemical Synthesis". Advances in Science and Technology, 2022, 119, 53–59.
[30] Saadi, B., Rahmane, S., Temam, E. G., "Structural, optical and electrical properties of spray deposited indium-doped Cr_2O_3 thin films". Journal of Optics (India), 2024, 53, 582–589.
[31] Mekkaoui, A., Temam, E. G., Rahmane, S., Gasmi, B., "A New Study on the Effect of Pure Anatase TiO_2 Film Thickness on Gentian Violet Photodegradation Under Sunlight: Considering the Effect of Hole Scavengers". Trends in Sciences, 2023, 20, 3766.
[32] Guettaf Temam, E., Djani, F., Rahmane, S., Ben Temam, H., Gasmi, B., "Photocatalytic activity of Al/Ni doped TiO_2 films synthesized by sol-gel method: Dependence on thickness and crystal growth of photo-catalysts". Surfaces and Interfaces, 2022, 31, 102077.
[33] Akkera, H. S., Sivakumar, P., Bitla, Y., Vanga, G., Kambhala, N., Naveen, C. S., Reddy, T. R. K., Reddy, G. S., "Structural, electrical, and optical properties of spin-coated Bi:SnO_2 transparent conducting oxide thin films". Physica. B. Condens. Matter., 2022, 638, 413839.
[34] Soumya, S. S., Xavier, T. S., "Effect of cobalt doping on the microstructural, optical and electrical properties of SnO_2 thin films by sol-gel spin coating technique". Physica. B. Condens. Matter., 2022, 624, 413432.
[35] Tiwari, A., Sahay, P. P., "Modification in the physical properties of nanocrystalline ZnO thin films by Sn/Ni co-doping for transparent conductive oxide applications". Physica. B. Condens. Matter., 2022, 629, 413638.
[36] Kumar, Y. B. K., Nagamalleswari, D., Babu, G. S., "Deposition of Cu_2ZnSnS_4 thin film at different solution flow rates". Physica. B. Condens. Matter., 2022, 645, 414263.
[37] Anne Sarah Christinal, R., Prakash, I., Chakravarty, S., Leo Rajesh, A., "Spray pyrolysed Cu_2ZnSnS_4 thin film photovoltaic cell fabricated using cost effective materials". Physica. B. Condens. Matter., 2022, 637, 413911.
[38] Kaushik, A., "Synergetic Effect of Sn 3^+ on Structural, Optical and Dielectric Properties of ZnO Nanostructures". Jñānābha, 2022, 52, 111–119.
[39] Roguai, S., Djelloul, A., "Structural, micro-structural, and optical properties of ZnO thin films prepared by spray pyrolysis". Algerian Journal of Renewable Energy and Sustainable Development, 2022, 4, 94–100.
[40] Sukmawati Arsyad, W., Angga Anugerah, M., Aba, L., Usman, I., Fisika dan Aplikasinya, J., "THE Effect of Variation Concentration and Deposition Parameter to the Optical Characteristics and the Crystallite Properties of Zinc Oxide". Spektra: Jurnal Fisika dan Aplikasinya, 2022, 7, 39–50.
[41] Rajan, A., Gupta, V., Arora, K., "Thickness dependent ultraviolet photoconductivity studies on sol-gel derived zinc oxide (ZnO) films". Mater. Today. Commun., 2023, 35, 105507.
[42] Anjum, A., Ahmed, R., Umar, Z. A., Azzam, S., Hussain, T., Sarwar, M. N., Baig, M. A., "Structure and defects-related optical properties of highly (002)-oriented zinc oxide thin films". Physica. B. Condens. Matter., 2022, 644, 414195.
[43] Morgante-Guandalini, N. C., Perez-Quintana, I. V., Daza, L. G., Acosta, M., Méndez-Gamboa, J., Muñoz, B. C., Castro-Rodríguez, R., "Vertical nanostructures thin films of CdS and CdTe using low temperatures GLAD". Physica. B. Condens. Matter., 2023, 666, 415075.
[44] Babalola, A. V., Oluwasusi, V., Owoeye, V. A., Emegha, J. O., Pelemo, D. A., Fasasi,

[DOI: 10.22068/ijmse.4142]

A. Y., Gurku, U. M., Alayande, S. O., Yusuf, S., Saje M, B., "Effect of tin concentrations on the elemental and optical properties of zinc oxide thin films". Heliyon, 2024, 10, e23190.

[45] Kumar, M., Pandey, P. S., Ravi, B., Kumar, B., Prasad, S. V. S., Singh, R., Choudhary, S. K., Singh, G. K., "Impact of Sn-doping on the optoelectronic properties of zinc oxide crystal: DFT approach". PLOS One, 2024, 19, e0296084.

[46] Abdullah, M., "Enhanced the Physical Properties of Thin Films by Doping Zinc Oxide with Tin Prepared by the Pyrolysis Technique". Journal of Kufa-Physics, 2023, 15, 46–53.

[47] Boufelgha, F., Zellagui, R., Benachour, M. C., Brihi, N., Dehdouh, H., Saeed, M. A., "Structural, morphological and optical properties of Sn doped zinc oxide thin films synthesis by sol-gel method for photocatalytic applications". Phys. Scr., 2023, 98, 085924.

[48] Ashour, A., Assem, E. E., Shaaban, E. R., "Investigation of dilute aluminum doped zinc oxide thin films: structural and morphological properties for varies applications". Journal of Ovonic Research, n.d., 18, 699–711.

[49] Sharma, H., Kumar, S., Yadav, J., Prasad, J., Singh, M., "Effect of Sn-incorporation on the Structural and Optical Properties of ZnO Thin Films Prepared by Sol-Gel Method". Oriental Journal of Chemistry, 2023, 39, 1540–1546.

[50] Alrefaee, M., Singh, U. P., Das, S. K., "Growth of Aluminum Doped Zinc Oxide Nanostructure Thin Films by Non conventional Sol-Gel Method". Macromol. Symp., 2022, 402, 2100350.

[51] Hallani, G. El, Khuili, M., Fazouan, N., Liba, A., Makarim, H. A. El, Atmani, E. H., "Experimental and DFT investigations of Al-doped ZnO nanostructured thin films". Chemical Physics Impact, 2024, 8, 100648.

[52] Ganesh Kumar, K., Balaji Bhargav, P., Ahmed, N., Balaji, C., "Influence of Sn Doping on the Structural, Morphological, Optical and Photocatalytic Functionality of ZnO Nanostructures". Transactions on Electrical and Electronic Materials, 2021, 22, 717–724.

[53] Afifah, F., Tjahjono, A., Ridhova, A., Maulida, P. Y. D., Noviyanto, A., Aryanto, D., "Influence of Al and Cu Doping on the Structure, Morphology, and Optical Properties of ZnO Thin Film". Indonesian Journal of Chemistry, 2023, 23, 44–52.

[54] Alqaisi, M. M., Ghazai, A. J., "Structural properties of pure and Sn doped ZnO thin film prepared using sol-gel method". J Phys Conf Ser, 2021, 1999, 012051.

[55] Bedia, F. Z., Bedia, A., Maloufi, N., Aillerie, M., "Doped ZnO Thin Films Properties/Spray Pyrolysis Technique". Advanced Structured Materials, 2020, 128, 107–119.

[56] Munna, N., Abdur, R., Islam, R., Bashar, M. S., Farhad, S. F. U., Kamruzzaman, M., Aziz, S., Shaikh, M. A. A., Hossain, M., Jamal, M. S., "Influence of Sn doping on the optoelectronic properties of ZnO nanoparticles". Nanoscale. Adv., 2023, 5, 4996–5004.

[57] Ahmed, G., Hasaneen, M. F., Mohamed, W. S., M. Ali, H., Ibrahim, E. M. M., "The Effect of Al and Sn Doping on the Optical and Electrical Properties of ZnO Nano-structures". Sohag Journal of Sciences, 2024, 9, 81–85.

[58] Deyu, G. K., Muñoz-Rojas, D., Rapenne, L., Deschanvres, J. L., Klein, A., Jiménez, C., Bellet, D., "SnO_2 Films Deposited by Ultrasonic Spray Pyrolysis: Influence of Al Incorporation on the Properties". Molecules, 2019, 24, 2797.

[59] Jongprateep, O., Meesombad, K., Techapiesancharoenkij, R., Surawathanawises, K., Munprom, R., "Effects of Sn Concentration on Chemical Composition, Microstructure and Photocatalytic Activity of Nano-particulate Sn-Doped TiO_2 Powders Synthesized by Solution Combustion Technique". Key. Eng. Mater., 2018, 766, 191–196.

[60] Sivarama Prabhu, P., Kathirvel, P., Maruthamani, D., Ram, S. D. G., "Enhanced photocatalytic activity of zinc oxide and tin doped zinc oxide nanoparticles synthesized by direct injection flame synthesis". Inorganic and Nano-Metal Chemistry, 2023, 55, 401-412.

[61] Ahmed, G., Mohamed, W. S., Hasaneen, M. F., Ali, H. M., Ibrahim, E. M. M., "Optical, structural, electrical and photo-

[DOI: 10.22068/ijmse.4142]

catalytic properties of aluminum doped zinc oxide nanostructures". Opt. Mater. (Amst.), 2023, 140, 113880.

[62] Saxena, G., Salmani, I. A., Khan, M. S., Khan, M. S., "Impact on the Structural, Morphological Properties, and Band Gap Tuning on Zinc Oxide Nanoparticles Substituted By Aluminum". ECS Journal of Solid State Science and Technology, 2023, 12, 081003.

[63] Al-Hardan, N. H., Hamid, M. A. A., Firdaus-Raih, M., Keng, L. K., "Aluminium-Modified ZNO Nanoparticles Synthesized Through Co-Precipitation". Jurnal Teknologi (Sciences & Engineering), 2022, 84, 9–14.

[64] Tonka, M., Guzelcimen, F., Baydogan, N., "Influence of Al content on microstructure and optical transmittance of sol-gel dip-coated ZnO films". Synthesis and Sintering, 2022, 2, 105–109.

[65] Marotti, R. E., Bojorge, C. D., Cánepa, H. R., Badán, J. A., Dalchiele, E. A., "Absorption edge shift and broadening in nanostructured Al doped ZnO thin films". Physica. E. Low. Dimens. Syst. Nanostruct., 2024, 162, 116008.

[66] Petrov, V. V., Ignatieva, I. O., Volkova, M. G., Gulyaeva, I. A., Pankov, I. V., Bayan, E. M., "Polycrystalline Transparent Al-Doped ZnO Thin Films for Photosensitivity and Optoelectronic Applications". Nanomaterials, 2023, 13, 2348.

[67] Mishra, P. N., Mishra, P. K., Pathak, D., "The Influence of Al Doping on the Optical Characteristics of ZnO Nanopowders Obtained by the Low-Cost Sol-Gel Method". Chemistry, 2022, 4, 1136–1146.

[68] Bouacheria, M. A., Djelloul, A., Adnane, M., Larbah, Y., Benharrat, L., "Characterization of Pure and Al Doped ZnO Thin Films Prepared by Sol Gel Method for Solar Cell Applications". J. Inorg. Organomet. Polym. Mater., 2022, 32, 2737–2747.

[69] Ennaceri, H., Taleb, A., Boujnah, M., Khaldoun, A., Ebothé, J., Ennaoui, A., Benyoussef, A., "Theoretical and experimental studies of Al-doped ZnO thin films: optical and structural properties". J. Comput. Electron., 2021, 20, 1948–1958.

[70] Ranjbari, A., Yu, J., Kim, J., Kim, J., Park, M., Kim, K. H., Heynderickx, P. M., "Fundamental kinetic modeling of dye sensitization photocatalysis by oxygen vacancy enriched ZnO for the quantification of degradation by catalyst or dye sensitizer". Appl. Surf. Sci., 2024, 659, 159867.

[71] Sa-nguanprang, S., Phuruangrat, A., Thongtem, T., Thongtem, S., "Preparation of Visible-Light-Driven Al-Doped ZnO Nanoparticles Used for Photodegradation of Methylene Blue". J. Electron. Mater., 2020, 49, 1841–1848.

[72] Bhatti, M. A., Almani, K. F., Shah, A. A., Tahira, A., Chana, I. A., Aftab, U., Ibupoto, M. H., Mirjat, A. N., Aboelmaaref, A., Nafady, A., Vigolo, B., Ibupoto, Z. H., "Renewable and eco-friendly ZnO immobilized onto dead sea sponge floating materials with dual practical aspects for enhanced photocatalysis and disinfection applications". Nanotechnology, 2023, 34, 035602.

[73] Kulis-Kapuscinska, A., Kwoka, M., Borysiewicz, M. A., Wojciechowski, T., Licciardello, N., Sgarzi, M., Cuniberti, G., "Photocatalytic degradation of methylene blue at nanostructured ZnO thin films". Nanotechnology, 2023, 34, 155702.

[74] Gogoi, D., Das, T. D., "The role of a highly optimized approach with superior transparent conductive oxide anode towards efficient organic solar cell". Phys. Scr., 2023, 98, 085908.

[75] Modi, S., Yadav, V. K., Amari, A., Alyami, A. Y., Gacem, A., Harharah, H. N., Fulekar, M. H., "Photocatalytic Degradation of Methylene Blue Dye from Wastewater by Using Doped Zinc Oxide Nanoparticles". Water, 2023, 15, 2275.

[76] Vallejo, W., Diaz-Uribe, C. E., Duran, F., "Kinetic and Thermodynamic Study of Methylene Blue Adsorption on TiO_2 and ZnO Thin Films". Materials, 2023, 16, 4434.

[77] Barakat, M. A., Kumar, R., Halawani, R. F., Al-Mur, B. A., Seliem, M. K., "Fe_3O_4 Nanoparticles Loaded Bentonite/Sawdust Interface for the Removal of Methylene Blue: Insights into Adsorption Performance and Mechanism via Experiments and Theoretical Calculations". Water, 2022, 14, 3491.

[78] El-Aassar, M. R., Tamer, T. M., El-Sayed, M. Y., Omer, A. M., Althobaiti, I. O., Youssef, M. E., Alolaimi, R. F., El-

[DOI: 10.22068/ijmse.4142]

Agammy, E. F., Alruwaili, M. S., Rabhy, O. O., Mohy-Eldin, M. S., "Development of Azo Dye Immobilized Sulfonated Poly (Glycidyl Methacrylate) Polymer Composite as Novel Adsorbents for Water Treatment Applications: Methylene Blue Immobilization Isotherm, Kinetic, Thermodynamic, and Simulations Studies". Molecules, 2022, 27, 8418.

[DOI: 10.22068/ijmse.4142]